

# EXPERIMENTAL EVALUATION OF A HIGH-SPEED PERMANENT-MAGNET MACHINE

Copyright Material IEEE  
Paper No. PCIC-()

Daniel M. Saban, PE PhD  
Senior Member, IEEE  
Direct Drive Systems  
12880 Moore St.  
Cerritos, CA 90703  
USA  
saban@ieee.org

Cassandra Bailey  
Member, ASME  
Direct Drive Systems  
12880 Moore St.  
Cerritos, CA 90703  
USA  
cbailey@directdrivesystems.net

Delvis Gonzalez-Lopez, PhD  
Member, IEEE  
Direct Drive Systems  
12880 Moore St.  
Cerritos, CA 90703  
USA  
dgonzalez@DirectDriveSystems.net

Ladislau Luca PhD  
Member, ASME  
Direct Drive Systems  
12880 Moore St.  
Cerritos, CA 90703  
USA  
lluca@DirectDriveSystems.net

**Abstract** - This paper presents the experimental evaluation of a high-speed, directly-coupled, multi-megawatt permanent-magnet machine. The maximum, continuous operating speed of the machine being evaluated is 15 krpm to match the shaft speed of compressors and turbines of up to 8 MW in targeted petroleum and chemical industry applications. The machine is characterized by high power-density and high efficiency. The design parameters and the predicted performance are corroborated by component, no-load, loaded and short-circuit tests. The thermal model and the cooling system design are evaluated and calibrated by the temperatures registered during the tests. The total measured losses and the allocation of losses across components is compared with the losses predicted by various analytical and numerical models.

*Index Terms* — Permanent magnet, high speed, synchronous, motor, generator

## I. INTRODUCTION

High-speed machines have become an increasingly attractive design solution in applications where it is desirable to eliminate gearboxes and their associated accessory systems. For example, High-speed electric motors with variable speed drives have been shown to have an advantage over gas turbines as a prime mover for natural gas compressor applications when both environmental and economic factors are considered [1] [2]. Also, power generation when directly coupled to a gas turbine has been considered with high-speed machines. High-speed machines can be operated at frequencies an order of magnitude above line frequency. This high-speed operation allows the machines to be smaller than conventional machines in the same power rating which yields significantly higher power density than with a conventional alternative. Due to the better power-to-weight ratio, smaller size, and higher efficiency compared to induction machines, high-speed permanent-magnet (PM) machines are a new topology being considered for sub-sea, off-shore and ship-board applications [3] [4]. Both synchronous (PM or wound-field) and asynchronous (induction) machines have been considered for these applications, however there are significant differences between these machines that warrant discussion.

The wound-field synchronous machines discussed by LaGrone [2] and Gilon [5] were discounted because of the complex rotor construction typical of wound-field synchronous

machines. PM synchronous machines do not suffer from many of the same difficulties, as they do not have field winding and a rotating rectifier. In addition, the modern synchronous PM machine designed for high speed and high power applications differs from its lower power brethren, such as the machine topologies studied by Melfi [6] and Bianchi [7].

High-speed PM machines typically have surface-mounted magnets and are sleeved. Laminated rotor cores and/or embedded magnets do not offer either the radial stiffness or mass containment required for many applications. The sleeve provides the containment and a solid rotor core, or hub, provides stiffness. Common sleeve materials are non-magnetic high-strength alloys [3], pre-molded graphite composite, and wound-in-place carbon fiber [8]. Of these, the carbon fiber winding offers the highest strength while providing minimal conducting path for eddy currents induced by air-gap flux disturbances. High-speed induction machines have also been presented with a solid rotor construction to address the rotor robustness issues [9].

While Arkkio [9] was primarily focused on high-speed applications not more than one or two megawatts, the observation that induction machines will require a larger diameter than an equivalent PM machine should not be lost on the reader. As the power rating becomes higher, the rotor speeds become lower, but the diameters grow. Arkkio suggests that the rotor tip speed of 250 m/s to be the upper limit for applying PM machines in favor of solid rotor induction machines. Gilon [5] limits the useful range of wound-field synchronous machines to 8000 rpm but does not tie that to a rotor diameter, or power rating.

Arkkio's [9] assessment that solid rotor induction machines suffer from both poor efficiency and low power factor when compared to PM machines is corroborated. Gilon [5] cites the low efficiency of solid rotor induction machines and Walter [9] presents performance data for such a machine that shows even at partial load the power factor is quite low (less than 0.7). However, it is not clear how much power factor reduction is due to the selection of the rotor construction and how much is due to the choice of pole count (a two-pole machine versus the four-pole machines presented by Weeber [3] and Bailey [8]). The typical trade-off between two-pole machines and four-pole machines is between power factor and efficiency, since two-pole machines operate at half the frequency of four-pole machines for the same shaft speed, but tend to have higher aspect-ratio stator slots and longer end turns. In addition, two-

pole machines will tend to be physically larger for the same power rating when the rotor diameter is held constant.

This paper presents the experimental evaluation of a permanent-magnet machine prototype targeted for 8 MW at 15 krpm. An early version of this design was presented in [8]. The equivalent circuit parameters obtained from open-circuit (OC), short-circuit (SC) and zero-power factor (ZPF) testing are compared with finite element (FE) results and the results are used to improve the assumptions in the FE model. Short-circuit testing provided the waveform used to predict the transient and sub-transient reactance. Stator-only (three-phase inductor) testing provided a means to calibrate the contact resistance used in the thermal model, at thermally stable current loadings not available in other early test configurations. Full-speed testing as a generator with a passive 3 MW load was carried out and the results are compared directly to the developed equivalent circuit and thermal models.

## II. TESTS AND RESULTS

### A. Equivalent Circuit Model

A standard exists [11] for testing synchronous machines, however many of the tests assume an adjustable field as with a wound-field synchronous machine. Tests for a PM synchronous machine can be adapted directly where a constant field is allowed. In particular the no-load loss test, the short-circuit test, and open-circuit voltage tests can be preformed. Fortunately this is enough for a simple equivalent circuit model. For PM machines the separate-drive method can be used to obtain the open circuit voltage ( $V_{OC}$ ) and no-load losses from no-load generator mode. The retardation method is used for total no-load losses.

An open-circuit generator test was carried out and terminal voltage of the prototype was recorded at several speeds. With PM machines the excitation flux, cannot be removed and therefore the friction and windage loss cannot be separated from iron loss and copper eddy loss. The total no-load losses were obtained, as is explained below, from spin-down operation.

The sudden short-circuit test presented in [9] was used to obtain the transient and sub-transient parameters from the current waveforms and the open-circuit voltage immediately before the sudden short circuit.

The equivalent circuit parameters were calculated from these test results and are shown in Fig. 1. The synchronous inductance ( $L_s$ ) was calculated for several speeds and similar values were obtained, as expected. For the rated speed (15 krpm with a frequency,  $f$ , of 500 Hz)  $X_s$  is  $2.2 \Omega$ , calculated from (1).

$$X_s = 2\pi \cdot f \cdot L_s \quad (1)$$

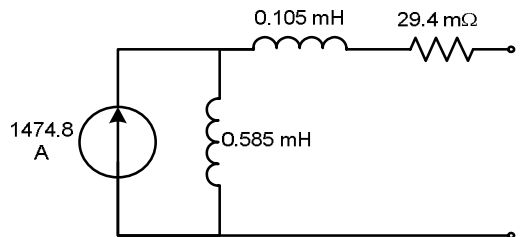
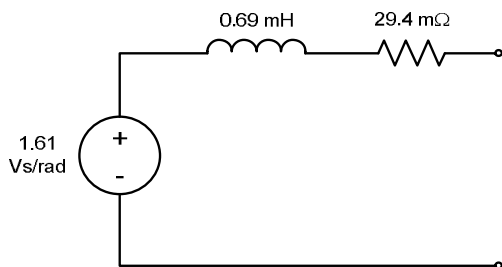


Fig 1. Simple voltage driven per phase equivalent circuit  
The open-circuit voltage is expressed as the speed dependant voltage source of Fig. 1, the open-circuit voltage constant,  $K_v$  (1.61) must be multiplied by the rotational speed in radians per second to arrive at the per-phase open circuit voltage.

Although the voltage-driven equivalent-circuit model is commonly used a current source model can also be used [12]. The parameters of such model were calculated for the presented machine and are shown in Fig. 2. The synchronous inductance is separated into the magnetizing and leakage components. The magnet is represented as a current source as is more common in electromagnetic field analysis.

Fig 2. Simple current-driven per phase equivalent circuit

Both equivalent circuit models are most valid at or near the frequency and current that tests were performed at. The parameters can vary with saturation, temperature and frequency, and these effects are typically included in a more detailed model. In general, more detailed models are used to predict machine parameters prior to build and test. These models can be lumped parameter (LP) models, finite element (FE) models or some hybridization of the two.

A two-dimensional (2D) FE analysis (transient with motion) was carried out to predict the open circuit voltage before machine build, and then again after test with the magnet strength adjusted to match the test. This parameter is very sensitive to the magnet material properties which vary with temperature and are not precisely well known prior to fabrication even by the manufacturer. Table I compares the FE results with the measured line-to-line voltage. The first row shows the predicted induced voltage from initial FE analysis using magnet material data supplied by the manufacturer. The second row contains the value of  $V_{OC}$  from an FE model with the magnet strength corrected from tests results. The values presented are for 15 krpm, however open-circuit voltage varies linearly with speed with close correlation.

TABLE I  
OPEN-CIRCUIT VOLTAGE AT 15 krpm

	$V_{OC}$ [V]
Initial FE prediction, 20°C	4685
Corrected FE results, 20°C	4392
Measured	4378

However for direct measurement, the line-to-line voltage scaled by the speed in rotations per minute is more convenient because of this linearity. The open-circuit voltage,  $V_{OC}$  was

measured for a complete speed range from no-load generator tests and normalized for speed, as depicted in Fig. 3.

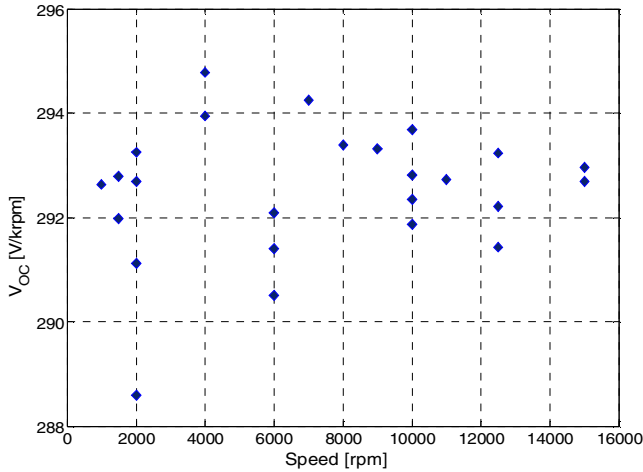


Fig 3. Measured open circuit voltage.

### B. Short Circuit Transient Response

Several sudden-short-circuit faults were imposed across the machine terminals, with the machine operating as a generator at low speed (2 krpm). A typical, measured current characteristic is shown in Fig. 4.

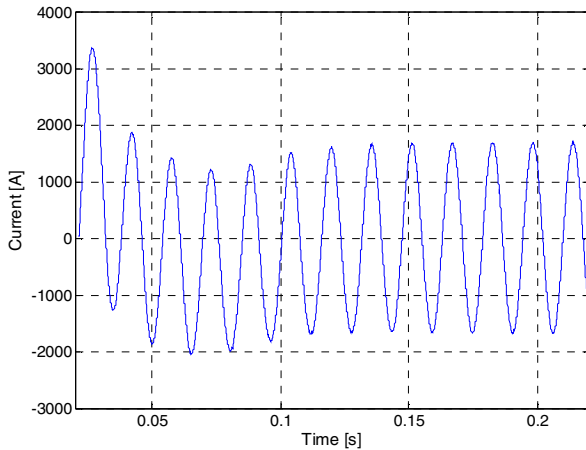


Fig 4. Measured short circuit current

During the short-circuit tests the stator current is only limited by the stator impedance; a high armature-reaction flux is imposed in the axis aligned with the highest flux density of the rotor magnets (the direct, or d-axis). In a poorly designed machine this condition can cause an irreversible degradation of the magnetic properties [13]. Therefore, is important that the machine will avoid demagnetization during the short circuit condition.

Table II shows the average open-circuit voltage measured before and after short-circuits testing. The total operation time under short-circuit condition was three hours and ten minutes.

During this test three-phase short-circuits were imposed 13 times at the machine terminals. No observable demagnetization has occurred. The large magnetic gap (i.e., the mechanical air gap + sleeve + magnet) imposes a high reluctance path to the armature-reaction flux and reduces the risk of demagnetization. The samarium cobalt magnets are chosen specifically for their high temperature operation and resiliency to demagnetization. These two factors contributed to the resiliency under the fault condition.

TABLE II  
NORMALIZED AVERAGE OPEN-CIRCUIT VOLTAGE CONSTANT MEASURED BEFORE AND AFTER SHORT CIRCUIT TESTS

	Before SC Test	After SC Test
$V_{OC}$ [V/krpm]	292.93	292.19

The total flux is reduced in a short-circuit test because the stator current produces a demagnetizing flux that directly opposes the rotor excitation. Therefore, a low saturation condition is present in the magnetic circuit. The calculated value of the steady-state unsaturated reactance ( $X_{US}$ ) is compared with FE results in Table III.

TABLE III  
UNSATURATED REACTANCE ( $X_{US}$ )

Speed [rpm]	$X_{US}$ [ $\Omega$ ]	$L_{US}$ [mH]
At 2000 (FE)	0.272	0.650
At 2000 (SC Test)	0.276	0.660
At 3000 (FE)	0.408	0.649
At 3000 (SC Test)	0.415	0.660
At 15000 (FE)	2.06	0.656

Table IV shows the transient ( $L_d'$ ) and sub-transient ( $L_d''$ ) inductances obtained from the short-circuit test and the calculated equivalent inductance at 15 krpm. There is negligible difference in these quantities due to rotational speed, supporting key assumptions regarding linearity with respect to frequency (especially for these unsaturated quantities), as with the open-circuit voltage.

TABLE IV  
TRANSIENT AND SUB-TRANSIENT REACTANCE

	L [mH] at 2.0 krpm	L [mH] at 15.0 krpm
Transient	0.525	0.525
Sub-transient	0.453	0.452

The transient ( $X_d'$ ) and sub-transient ( $X_d''$ ) reactance per unit of the machine base impedance are presented in Table V.

TABLE V  
AS TESTED PARAMETERS IN PER UNIT,  $X_d'$  AND  $X_d''$

	Prototype
$X_d'$ [pu]	0.525
$X_d''$ [pu]	0.453

### C. Thermal Model and Stator-only Test

The heat generated in the machine during operation is removed by a two-part cooling system; liquid cooling provides cold flow through the stator outer- diameter cooling-jackets and forced air cools the air gap and end-turns of the stator winding.

In normal operation, a blower pumps air to the mid-stack of the stator, where it splits and flows toward the ends through the air gap. A second blower forces the air over the stator winding end-turns. This was the cooling arrangement selected for this prototype unit and may not be indicative of a production machine.

The heat transfer in typical electrical machines is by conduction, convection and radiation. The relatively small temperature difference between solid components of the prototype allows radiation to be neglected in the theoretical analysis. The heat transfer coefficient of the end-turns and the contact resistance between stator core and cooling jacket significantly influence the cooling system effectiveness, but are difficult to determine analytically.

Prior to the complete build of the prototype machine, a “stator-only” test used ambient air flow and the water cooling system to choose a stator contact resistance for the thermal model. Current magnitudes of varying frequency and magnitude were injected into the stator winding. Stable temperatures were measured with thermocouples installed on the surfaces of the end-turns and resistance temperature detectors (RTDs) in the stator slots. Measured temperatures were corrected for the temperature gradient across the insulation for comparison with the predicted copper temperature.

A computational fluid dynamics (CFD) model was used to validate the thermal model for a simulated operating condition. The model segregated the stator iron and copper losses. Fig. 5 shows the temperature distribution obtained from CFD analysis.

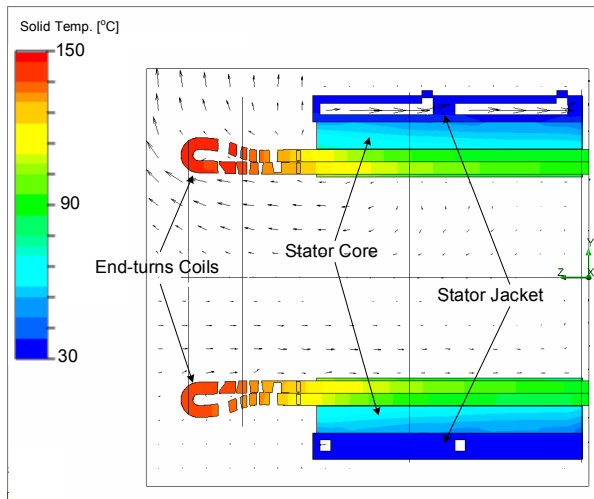


Fig 5. Stator temperature distribution (Longitudinal view).

The maximum stator temperature occurs in the coil end-turns, which are primarily cooled by natural convection in this test. The coil slot sections are cooled mainly by conduction to

the cooling jacket through the stator laminations. Table VI shows the calculated and measured stator coil temperatures.

TABLE VI  
CALCULATED AND MEASURED STATOR COIL TEMPERATURES

	End-turns	Inside the slot
CFD Analysis	140.0 °C	105.1 °C
Measured	137.0 °C	105.0 °C

The total losses are obtained by calculating the input power from the voltage and current measurements. The copper conductors produce ohmic loss from the net current at the operating frequency and eddy-current loss due to the changing magnetic field impressed upon them. There is an additional loss component from the proximity of the conductor strands. Rather than build a strand-by-strand FE model of the stator winding to predict the iron loss, a simple coil model (Fig. 6) was used for iron loss calculation for this condition. The copper loss is the difference between the iron loss and the measured input power. Since the prototype was tested in this configuration without the rotor, effectively as a three-phase inductor, the input power is identically the output power. The power source in this test was the same power electronic drive used in later testing.

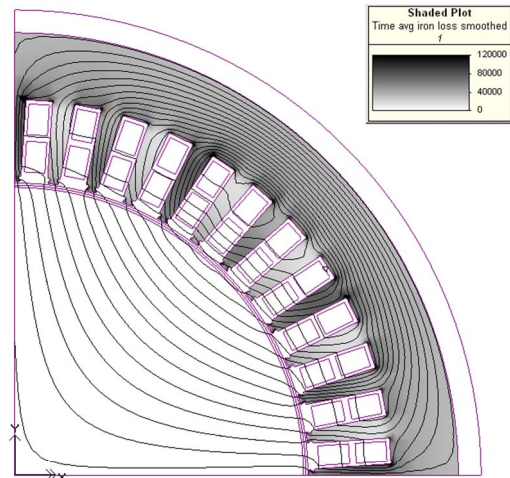


Fig 6. Iron loss distribution in the stator from FEA during stator-only testing

The total measured loss in the CFD model was used to find the loss distribution that produces the temperature profile observed during the test. The iron loss is taken from the FE model shown in Fig. 6 and distributed in the stator core. The copper loss is split between the portion of copper in the slots and the end-turn winding. The heat transfer coefficients and contact resistance used in the thermal model are adjusted empirically (within heuristic bounds) to obtain a final thermal model and loss distribution. A heat balance using the measured flow and temperature of the cooling liquid and the predicted heat removal via convection agreed with the total loss measured at the stator terminals. Table VII presents the loss allocation from the thermal model for this test condition.

TABLE VII  
LOSS SEGREGATION FOR STATOR-ONLY TEST

	Iron Loss [kW]	Slot Cu Loss [kW]	End-turn Cu Loss [kW]	Total losses [kW]
CFD Model	10.52	8.28	3.72	22.52

Limitations of the drive used during this testing prevented exploring the entire frequency and excitation range. The flux distribution in the stator under this condition is not the same as that seen under normal operation. The flux distribution and limited frequency and excitation range are not as significant as the fact that the total losses and stator temperatures are lower than expected in operation. A greater temperature rise above ambient would have provided better correlation for the thermal model.

#### D. No-load losses

The prototype was driven by a PM motor (rated for 22 krpm and 2 MW) during the no-load tests. The 2 MW motor was also run at no-load uncoupled from the prototype and total input power over the speed range were taken to be the no-load losses. The no-load losses of the driven 8 MW machine are calculated by subtracting the loss of the uncoupled 2 MW machine from the no-load loss measured during spin-down of the coupled machines. The power-electronic drive was open-circuited while running the machines at 15 krpm. The speed versus time during coast-down was used to calculate the energy stored in the system. Since the inertia of both machines is known, the kinetic energy can be calculated by,

$$E = \frac{(I_M + I_P) \cdot \omega^2}{2} \quad [\text{J}] \quad (2)$$

where  $I_M$  and  $I_P$  are the inertias of the 2 MW motor and the 8MW prototype respectively and  $\omega$  is the angular speed in rad/sec. The total power dissipated by the system is given by the decrease in kinetic energy with time. The no-load losses of the prototype were obtained as the difference between both running conditions.

The no-load loss segregation is a challenge in PM machines. The first step is to define the power allocation for open-circuit operation. The no-load losses are composed of total air gap loss due to the friction and windage; mechanical losses in bearings; and magnetic losses in the stator laminations and stator windings. Additionally second-order eddy-current losses may be present in components of the housing and bearing structure. Rotor eddy current losses for this mode of operation are calculated analytically and are found to be negligible. Fig. 7 depicts the no-load loss segregation up to 15 krpm.

The air-gap windage loss was calculated analytically for the complete speed range using the air gap dimensions and the temperature recorded during no-load tests. The measurement of the supply and outlet temperatures and mass-flow rate of the coolant were used to calculate the losses in the bearings. The difference between total no-load losses and air-gap and bearing losses are the total magnetic losses (iron loss and eddy-current losses in the stator coils). This analysis was the starting point to

distribute the losses in the thermal model to produce the same temperature profile recorded on the open-circuit test.

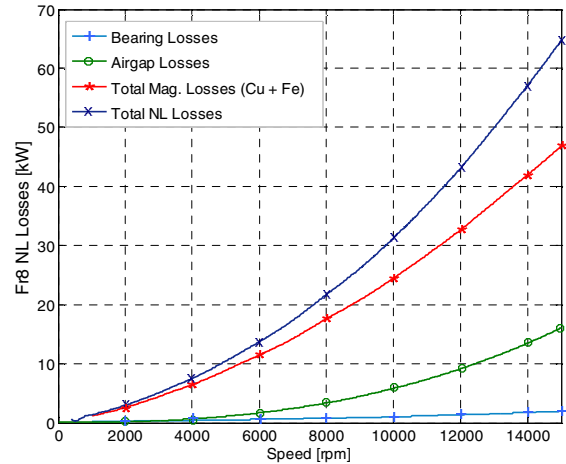


Fig 7. No-load loss segregation

The rotary excitation flux causes a significant loss in the stator coils due to the eddy-current effect. This loss component is directly dependent on the number of strands size and configuration. A multi-strand FE model was developed to estimate the eddy current losses at several frequencies. Fig. 8 shows the current density distribution for no-load generator at 15 krpm using the multi-strand FE model. Since the terminals are open-circuited, the current distribution is due solely to the eddy current from the rotating excitation flux.

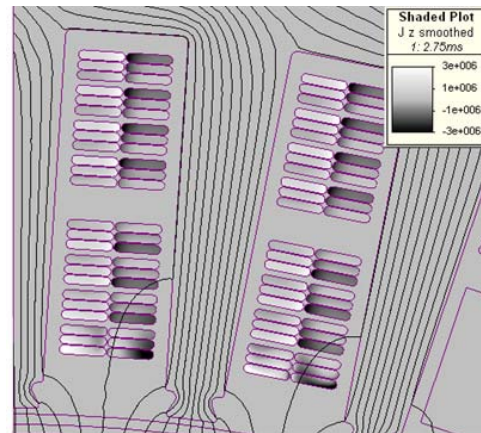


Fig 8. Current density distribution in the stator coils for the no-load generator case at 500 Hz, 15 krpm.

Black: +3 MA/m<sup>2</sup>  
White: -3 MA/m<sup>2</sup>

A number of analytical methods for the eddy current losses in the stator coils [14]-[17] were evaluated. The copper losses obtained from the FE model are compared in Table VIII with thermal model and analytical results.

Of the analytical eddy current calculation methods, only Shanks gives a result close the FE model. This was the only analytical method calibrated with test data, all other methods

were derived from first principles alone. The FE model used was strictly 2D and so only the portion of the winding in the slot was considered, although the strand placement and interconnection was faithful to the machine, as built. None of the methods approached the CFD model results.

TABLE VIII  
EDDY CURRENT LOSS IN STATOR COILS

f [Hz]	FE	CFD	Say [14]	Walker [15]	Shanks [16]	Fink [17]
100	0.32	1.58	18.13	0.08	0.22	4.08
300	2.39	7.47	23.96	0.72	1.99	36.74
400	3.99	11.71	29.07	1.23	3.53	65.34
500	5.91	16.80	35.63	1.98	5.52	102.05

A commercial LP model was also used to predict the no-load loss, as well as for various other load conditions. This model had been calibrated with some initial test data from other machines, but it assumes a uniform current distribution in the windings – in this case, zero current. The iron losses used in the LP model make use of the Steinmetz [18] coefficients interpreted from manufacturer supplied data [19].

Table IX compares the total machine loss distribution for the no-load condition obtained from CFD, FE and LP models.

TABLE IX  
NO-LOAD LOSS SEGREGATION AT 15 krpm, 500Hz

[kW]	Iron Loss	Slot Cu Loss	Windage	Total losses
<b>CFD Model</b>	29.9	16.8	16.3	63.0
<b>FE Model</b>	20.7	5.9	n/a	n/a
<b>LP Model</b>	24.9	0	20.0	44.9

The winding loss calculation for the LP model does not include the proximity, skin and eddy-current effects. This loss component is zero for open circuit case because is produced only by the Joule effect ( $I^2 \cdot R$ ). The windage loss in both models can be refined as they should be made to agree much more closely: the LP model used an assumed gap air temperature whereas the gap air in the CFD model agreed with test data. The iron loss allocation is within 20% among the three models. Although not desirable, this discrepancy is much less than the copper eddy losses (among these three models and the analytical methods). There can be some confounding between the iron loss and the windage losses since the highest loss density for the iron loss is at the stator tooth-tips, which is in close contact with the air-gap, where the windage is produced. Some of the windage loss is carried away via the tooth tips into the cooling jacket, so it is not surprising that the sum of windage and iron losses are very close between the CFD and LP models. The iron losses as calculated by the FE model are a function of the numerical calculation procedure, the details of the model and material properties. The FE and LP models should be in closer agreement in general, however the LP model assumes a particular flux distribution along pre-determined paths whereas the FE model calculates the expected flux distribution from the machine geometry and excitation in total. It is likely that the LP model uses slightly more pessimistic assumptions, but that both LP and FE models are using an optimistic representation of the material properties.

### E. Rotor Dynamics

A commercially available finite-element-analysis rotor-dynamics software package was used to predict the performance of the rotor assembly. The total system model includes the rotor, bearings, and squeeze-film dampers. The frame of the machine is considered infinitely rigid and is therefore not included in the analysis. The software was used to predict the systems' natural frequencies, both free-free and damped with corresponding mode shapes, and the dynamic response based on predicted imbalance.

The program lumps the mass and inertia of a defined area and creates nodes connected by massless beams. The rotor itself is modeled conservatively; the magnets and carbon fiber sleeve are modeled as a mass at the appropriate distance from the center of the shaft, however they are assumed to contribute no structural stiffness to the rotor. This conservative approach results in predicted natural frequencies that are lower than the actual, but this analysis method is still utilized to compensate for manufacturing variation. Previous experience also validates the approach that the segmented magnets and carbon sleeve do not contribute appreciably to the overall rotor stiffness.

In order to validate the rotordynamic model the rotor was hung vertically and subjected to a modal impact (Fig. 9). Again the predicted natural frequencies should be lower than the measured natural frequencies due to the conservative nature of the analysis.

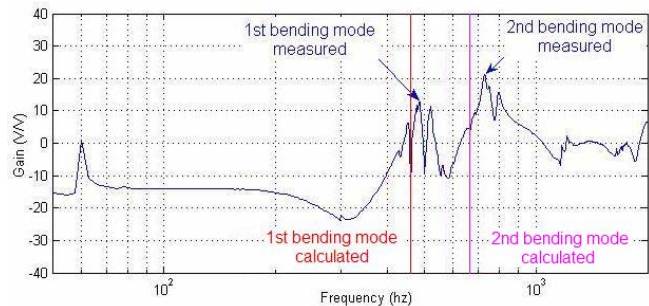


Fig 9. Rotor impact modal test results

The dynamic behavior of the rotor was continually monitored during testing at the outboard side of each bearing support on both the drive end and non-drive end of the machine. Three one-axis accelerometers were oriented vertically, horizontally, and axially at both ends for a total of six accelerometers. Proximity probes were oriented vertically and horizontally at both ends and additionally one probe was mounted axially at the non-drive end for rotor growth and total axial displacement monitoring. The proximity probe data was used to plot the rotor orbits. The predicted peak-to-peak displacement at either end was 0.00127 cm (0.5 mils) to 0.01143 cm (4.5 mils) when going through the rigid body modes and approximately .00254 (1.0 mils) at 15krpm, depending on the exact distribution of rotor imbalance. The observed displacement of the shaft during operation fell well within the predicted range (Figs. 10 & 11) at rotor thermal steady state. Prior to thermal steady state of the rotor vibration and displacement values measured were higher than measured at thermal steady state, however they stayed below the maximum predicted levels. Peak vibration measured at the non-drive end during operation

prior to thermal steady state of the rotor was less than 2 g (rms) at 15 krpm. The vibration at the drive end in all three orientations was less than 1.4 g (rms) at 15 krpm (Fig. 12). The dynamic behavior of the system was stable and acceptable for continued operation. Overall the rotor and bearing support system behaved close to predicted levels, confirming that the analysis method was appropriate for the design.

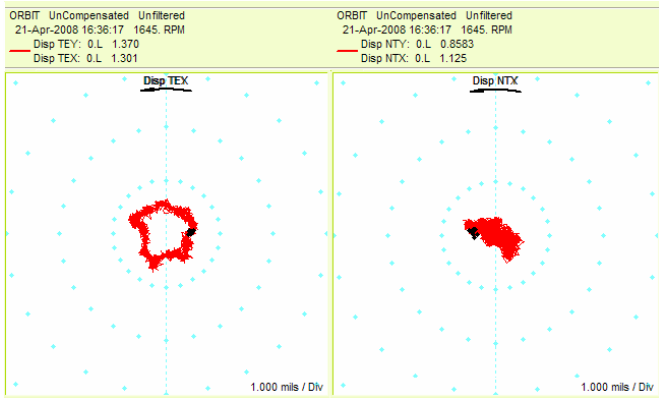


Fig 10. Drive End (left) and Non-Drive End (right) X-Y Orbit Plot at 1645 rpm

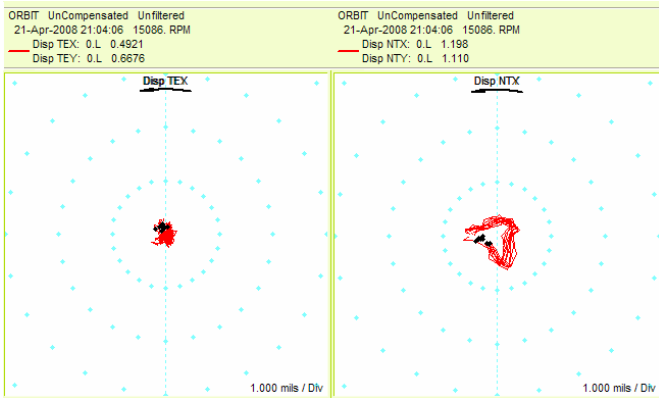


Fig 11. Drive End (left) and Non-Drive End (right) X-Y Orbit Plot at 15086 rpm

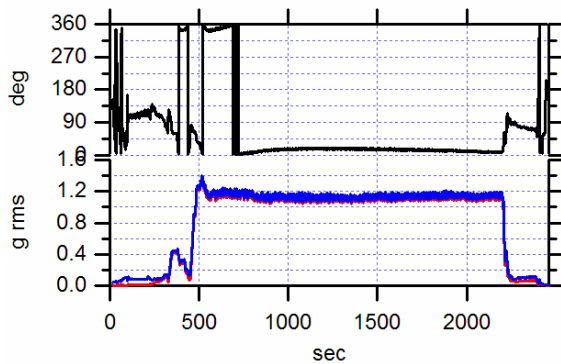


Fig 12. Drive End Vibration Bode Plot for a 40 minute test with a maximum rotor speed of 15 krpm between 500 sec and 2200 sec.

### III. 3 MW TESTING

Partial load tests were conducted using a resistive load bank and a gas turbine rated for 3 MW at 15 krpm to drive the prototype machine as a generator. Although the turbine is limited to continued operation under load to speed very close to 15 krpm, the resistive load bank can apply the load in steps as small as 125 kW. The load was increased stepwise from 125 kW up to 3 MW, providing several different operating points to compare to the equivalent circuit predictions.

Fig. 13 depicts the measured and predicted output power from the equivalent circuit parameters and the LP model. The close agreement between both data sets validates the equivalent circuit shown in Fig. 1. The LP model “passive load” case assumes a unity power factor, purely resistive load. The “active load” case assumes that the load power factor is adjusted such that the machine operates with the maximum power conversion.

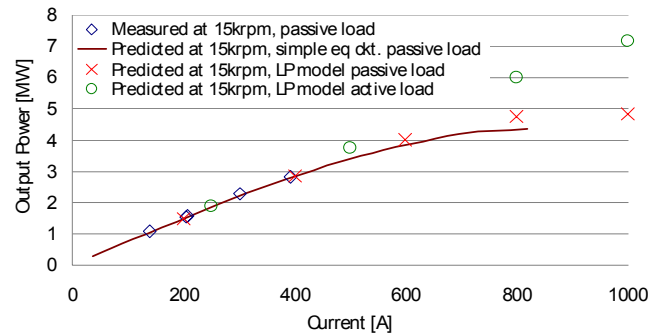


Fig 13. Predicted and measured output power at 15 krpm.

The simple equivalent circuit model uses a resistor in series with the output of the machine that includes the iron and copper loss and agrees more closely with the test data (and CFD) than the LP model. The iron-loss resistor would be better represented as a parallel resistor separate from the winding resistance. This improvement to the equivalent circuit model should provide better agreement with the LP model, at the cost of model simplicity. Retaining the level of model simplicity in Figs. 1 and 2 would require a different resistance for each frequency and excitation of interest (and a different inductance as well), which is useful for hand calculations around a will known operating point, but is exactly the reason why more rigorous LP models are employed for electric machine analysis.

The measured current in steady state at 15 krpm was 393 A and fed an electric load of slightly less than 3 MW. The analyses below are focused on that operation point. The FE model developed for calculation of the copper eddy-current losses for the no-load condition was excited to correspond with the 3 MW test. The resulting current density distribution is presented in Fig. 14.

Table X compiles the loss predictions for the FE, LP and CFD models. The FE method has been accepted as a viable means to predict eddy-current effects in rotating machines, the focus of research in this area has been to improve the details of the numerical formulation and computational efficiency of the problem, and not whether or not this is a viable approach [20]-

[22]. So it is surprising that the FE model predicts a significantly lower eddy-current loss than the CFD model supported with test data. It is noteworthy that the difference between the CFD and FE prediction of copper eddy-current loss is maintained between the no-load (Table VIII) and 3MW cases – this gives some insight into the problem. The effect of current loading appears to have been handled consistently between the two models, but resolving the discrepancy lies with understanding the no-load case. This suggests that if no-load testing is used as a baseline for loss allocation, then the effects of loading can be determined numerically (with the FE model).

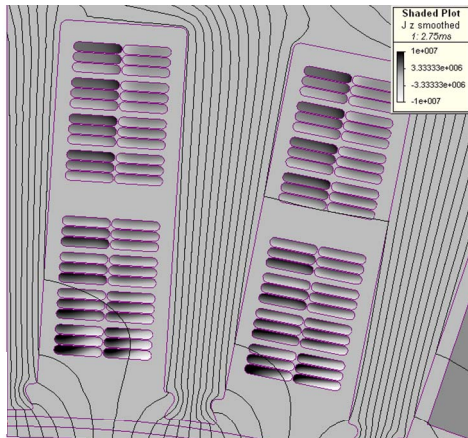


Fig 14. Current density distribution in the stator coils for the 3MW load generator case at 500 Hz, 15 krpm.  
 Black: +10 MA/m<sup>2</sup>  
 White: -10 MA/m<sup>2</sup>

TABLE X  
 LOSS SEGREGATION FOR 3 MW, 15 krpm OPERATION

	Iron Loss [kW]	Slot Cu Loss [kW]	End-turn Cu Loss [kW]	Windage [kW]	Total loss [kW]
<b>CFD Model</b>	33.60	21.2	1.77	17.80	74.37
<b>FE Model</b>	23.77	9.95	1.72	n/a	n/a
<b>LP Model</b>	24.46	1.91	1.71	20.0	48.08

The FE model and LP model agree better under load than under the no-load case. This is not surprising as the assumptions built into the LP model are expected to be skewed towards “normal” or loaded operation, as this is the condition typically of the most interest. The significant difference between the FE model and LP models (using similar material properties) and the CFD model suggests that the stator lamination material is more lossy than the material properties used in the FE and LP models would indicate.

The (2D) FE model losses allocated to the end-turns are derived from the LP model which does not consider skin effect. It could be conjectured that the total loss budget in the CFD model is misappropriated in this regard, were it not for the close correlation between measured and predicted temperatures (Table VI).

The allocation of losses is more important to the temperature rise prediction of specific components rather than to the power conversion calculation. The discrepancy in losses between the

FE and CFD models account for about 0.7% change in machine efficiency at 3 MW and less than 0.2% change in machine efficiency at 8 MW. However a change of a few kilowatts of loss in a given component is enough to raise the predicted temperatures a non-negligible amount.

#### IV. CONCLUSIONS

The mechanical model used for prediction of rotor dynamics agreed closely with measurements, given the conservative assumptions used. The method used can be applied to similar machines without relying on machine or component level testing for needed accuracy.

The thermal model utilizing computational fluid dynamics (CFD) was able to provide insight into the loss distribution within the machine when correlated with component test data. This physics-based model can be extended for machines of similar construction without loss of generality.

Analytical and numerical methods based on electromagnetic models, both lumped parameter (LP) and finite element (FE) proved to be inadequate for *a priori* loss prediction, especially at no-load. This is an area to be explored in greater detail since there are many factors that influence these predictions and not all loss mechanisms or all components of the electric machine were considered.

A combination of LP and FE methods can be used for reliable power conversion calculations. However, the simplest equivalent circuit models should be eschewed at higher excitation levels.

A loss budget above the initially predicted values should be maintained for prototypes developed without the benefit of similar machines to calibrate the analysis and design tools. The cooling system used for machine development can be oversized to compensate for discrepancies between initially predicted and as-built machine losses.

#### V. REFERENCES

- [1] B. M. Wood, C. L. Olsen, G. D. Hartzo, J. C. Rama, and F. R. Szenasi, “Development of an 11 000-r/min 3500-hp Induction Motor and Adjustable-Speed Drive for Refinery Service,” *IEEE Transactions on Industry Applications*, vol. 33 No. 3, pp 815-825, May/June 1997.
- [2] S. LaGrone, M. Griggs, and M. Bressani, “Application of a 5500 RPM high speed induction motor and drive in a 7000 HP natural gas compressor installation,” in *IEEE PCIC Conference Record*, 1992, pp 141-146.
- [3] K. Weeber, C. Stephens, J. Vandam, A. Gravame, J. Yagielski and D. Messervey, “High-Speed Permanent-Magnet Motors for Oil & Gas Industry,” *Proceedings of GT 2007 ASME Turbo Expo 2007: Power for Land and Air*, May 14-17, 2007, Montreal, Canada.
- [4] N. Shade, “New Compression and Power Application,” *Compressor Tech Two*, Mar 2008. pp 20-26.
- [5] Gilon, D. “Design and tests of a 6 MW, 10000 RPM induction motor,” *5th International Conference on Electrical Machines and Drives*, London, 1991, pp 6–10.
- [6] M. Melfi, S. Rogers, S. Evon, and B. Martin, “Permanent Magnet Motors for Energy Savings in Industrial Applications,” in *IEEE PCIC Conference Record*, 2006, No. PCIC-2006-11.
- [7] N. Bianchi, S. Bolognani and F. Luise, “Potentials and

- Limits of High-Speed PM Motors," *IEEE Transactions on Industry Applications*, vol. 40, No. 6, pp 1570-1578, Nov/Dec 2004.
- [8] C. Bailey, D. Saban and P. Guedes-Pinto, "Design of High-Speed, Direct-Connected, Permanent-Magnet Motors and Generators for the Petrochemical Industry," *IEEE PCIC Conference Record*, Sep 2007.
- [9] A. Arkkio, T. Jokinen, and E. Lantto, "Induction and Permanent-Magnet Synchronous Machines for High-Speed Applications," *Proceedings of the Eighth International Conference on Electric Machines and Systems, 2005 ICEMS 2005*, vol. 2, pp 871-876, Sep 2005.
- [10] H. Walter, A. Moehle and M. Bade, "Asynchronous Solid Rotors as High-Speed Drives in the Megawatt Range," *IEEE PCIC Conference Record*, Sep 2007.
- [11] IEEE 115-1995, *IEEE Guide: Test Procedures for Synchronous Machines*.
- [12] T. Sebastian, G. Slemmon and M. A. Rahman, "Modeling of Permanent Magnet Synchronous Motors," *IEEE Transactions on Magnetics*, vol. MAG-22, No. 5, pp 1069-1071, Sep 1986.
- [13] M. Rosu, A. Arkkio, T. Jokinen, J. Mantere and J. Westerlund, "Demagnetisation State Of Permanent Magnets In Large Output Power Permanent Magnet Synchronous Motor". *Electric Machines and Drives, 1999. International Conference IEMD '99*, pp 776-778, May 1999.
- [14] M. G. Say, *Alternating Current Machines*, Wiley 4<sup>th</sup> edition, 1976.
- [15] J. H. Walker, *Large Synchronous Machines*. Clarendon Press. 1996.
- [16] G. Shanks, "Stator Surface Per Watt (s/w)," *Internal Memo to J. Imbertson*, Feb 18, 1976.
- [17] D. G. Fink and W. H. Beaty, *Standard Handbook of Electrical Engineering*. McGraw-Hill 15<sup>th</sup> ed. 2007.
- [18] C. P. Steinmetz, "On the law of hysteresis – originally published 1892 and reprinted in," *Proceedings of the IEEE*, vol. 72, pp 196-221, Feb 1984.
- [19] T. J. E. Miller and M. I. McGilp, *PC-BDC 6.5 for Windows – Software*, SPEED Laboratory University of Glasgow, Glasgow, UK, 2004.
- [20] M. V. K. Chari and Z. J. Csendes, "Finite Element Analysis of the Skin Effect In Current Carrying Conductors," *IEEE Transactions on Magnetics*, vol. MAG-13, No. 5, Sep 1977.
- [21] M. V. K. Chari and Z. J. Csendes, "New Finite Element Techniques for Skin Effect Problems," *IEEE Transactions on Magnetics*, vol. MAG-18, No. 2, Mar 1982.
- [22] Á. Szücs and A. Arkkio, "Consideration of Eddy Currents in Multi-Conductor Windings Using the Finite Element Method and the Elimination of Inner Nodes," *IEEE Transactions on Magnetics*, vol. 35, No. 3, May 1999.

## VI. VITA

**Dan Saban** earned a BSEE degree from the University of Illinois - Urbana in 1992, a MSEE degree from Purdue University - West Lafayette in 1993 and a PhD degree in Electrical Engineering from the University of Wisconsin - Madison in 2006 where he specialized in electric motor analysis. Additionally, he holds an MSEE (2002) and a MSME (2003) from University of Wisconsin - Madison with focuses on power electronics and controls, respectively. He is currently the Director of Technology for Direct Drive Systems. Throughout his 16 year career (including time spent with General Electric and Hamilton Sundstrand) he has been involved in advanced electromagnetic design of electric machinery including new lamination and winding designs, design tool improvement, and both prototype and product family development for commercial, industrial and aerospace applications. Dr. Saban is a senior member of IEEE and a registered professional engineer in Indiana and Illinois.

**Cassandra Bailey** was graduated in 2003 from Northwestern University with a Bachelors of Science degree in Mechanical Engineering and is a member of ASME. She started her career as an Integrated Drive Generator Design Engineer with Hamilton Sundstrand designing an integrated variable-speed transmission and AC generator for various military aircraft applications. Currently, she is with Direct Drive Systems as a Project Engineer designing high-speed medium-voltage permanent-magnet machines.

**Delvis Gonzalez-Lopez** received the Electrical Engineer degree in 1997 and the Master in Science degree in 2001, from Central University of Las Villas, Cuba. He earned a Doctoral degree in Engineering Science/Electrical Engineering in 2006 from the University of Concepcion, Chile. Currently, he is an Electrical Engineer for Direct Drive Systems. Dr. Gonzalez is an IEEE Member and his research interests include design, optimization and control of electrical machines, primary permanent-magnet machines.

**Ladislau Luca** earned a MSME degree at the Energetic department of Polytechnic University of Bucharest, Romania and a PhD degree in 1981, at the same University, dealing with heat transfer in nuclear reactor cooling systems. During his engineering career he has been involved in thermal-hydraulic research, design and analysis of various equipment. He has created thermal analysis software and performed work regarding cold plates and heat exchangers used for cooling electronic equipments in aerospace, military and commercial industry.

At DDS, he is responsible for the thermal modeling and analysis of high-performance permanent-magnet machines including development of CFD models. He has been a member of ASME since 1992. His activity is reflected in 4 textbooks and more than 40 technical papers.